

# Fault Ride-Through Enhancement for Grid-Tied PV Systems With Robust Control

Yeqin Wang, *Student Member, IEEE*, and Beibei Ren , *Member, IEEE*

**Abstract**—In this paper, a new control structure is proposed for grid-tied photovoltaic (PV) systems where the dc bus voltage is regulated by the dc/dc converter controller, whereas the maximum power point tracking (MPPT) function and the power flow control are embedded into the dc/ac converter controller. A PV voltage-regulation is designed to build the linkage between MPPT function and power flow control. In this way, the dc/dc converter controller and the dc/ac converter controller are decoupled, which naturally provides the dc bus voltage protection. In particular, an uncertainty and disturbance estimator (UDE)-based current-mode controller (CMC) is proposed for accurate voltage regulation of the dc/dc converter. And a bounded-voltage power flow control strategy is proposed for the dc/ac converter to improve the existing UDE-based robust power flow control for ac voltage protection. The effectiveness of the proposed method is experimentally validated in a lab-environment grid-tied PV system platform with the fault ride-through capabilities. In addition, simulation studies are also provided to demonstrate the need of the PV voltage-regulation between MPPT and power flow control, and the advantages of the bounded-voltage design in the power flow control.

**Index Terms**—Bounded-voltage power flow control, dc bus voltage protection, fault ride-through, grid-tied photovoltaic (PV) systems, uncertainty and disturbance estimator (UDE).

## I. INTRODUCTION

SOLAR energy is very promising in future energy industry. One of the solar technologies, the photovoltaic (PV), can directly convert sunlight into electricity based on one or two layers of semiconducting materials. Since the sunlight is variable, and the output power of a PV source depends on the load condition, power electronic converters are essential for converting the dc power generated by PV sources into ac electrical grid with maximum power point tracking (MPPT) strategies [1]. In some previous works [2]–[4], the PV source is often used for battery charging or other dc applications. With the growing of solar industry, the grid integration of PV energy becomes popular [5]–[8]. In addition, most research for solar system focuses

on increasing the efficiency of the PV source with MPPT algorithms, e.g., in [9]–[11].

A typical topology for grid-tied PV systems has two processing stages through a dc/dc converter and a dc/ac converter, respectively, [1]. The dc/dc converter, usually a boost converter, converts the dc power with variable dc voltage of the PV source into a constant voltage dc bus [6], [7], [12], [13]. Then, the dc/ac converter converts the dc power of dc bus into the ac electrical grid. For the control of two processing stages for grid-tied PV systems, the MPPT function is usually embedded into the control of the dc/dc converter, and the dc bus voltage is regulated by the dc/ac converter in most literature, e.g., in [5]–[8]. The proportional-integral (PI) controller is usually adopted for the dc bus voltage regulation to generate a current reference or a power reference, then a current controller or a power controller is adopted for the dc/ac converter with ac grid integration. In this case, the dc bus voltage will increase due to the continuous operation of the dc/dc converter with the MPPT function when the faults happen in the dc/ac converter or grid side. Then, the power electronic devices might be broken down due to high dc bus voltage, as well as the PV sources. Though, a dc bus voltage protection unit is designed in most cases, the protection performance is limited by the response time and the designed voltage tolerance.

Since the duty cycle of the dc/dc converter is directly regulated by the MPPT algorithm and the dc bus voltage is regulated by dc/ac converter side, no robustness for the dc/dc converter control is introduced into grid-tied PV systems. And only the averaged relationship between input voltage and output voltage of the dc/dc converter is considered in previous controls of grid-tied PV systems, e.g., in [4], [8], [9], [14], however, the dc/dc boost converters are highly nonlinear [15], [16], discontinuous in time [15], and variable structure systems [15], also exhibit the nonminimum phase phenomenon [16], [17]. Another important issue for grid-tied PV systems is keeping the output voltage of the dc/ac converter within the given range for ac voltage protection, particularly, in the operation of islanded mode microgrid/smart grid [18]. Adding a saturation unit is a common way to maintain the given bound for the output voltage of the dc/ac converter, however, which often leads to instability and undesired oscillations due to the integrator windup [19], [20].

Different from most existing works [5]–[8], in this paper, a new control structure is proposed for grid-tied PV systems where the dc bus voltage is controlled by the dc/dc converter controller, whereas the MPPT function and the power flow control are embedded into the dc/ac converter controller. This naturally decou-

Manuscript received February 22, 2017; revised June 21, 2017; accepted July 21, 2017. Date of publication August 17, 2017; date of current version December 15, 2017. (Corresponding author: Beibei Ren.)

Y. Wang is with the National Wind Institute, Texas Tech University, Lubbock, TX 79409-1021 USA (e-mail: yeqin.wang@ttu.edu).

B. Ren is with the Department of Mechanical Engineering, Texas Tech University, Lubbock, TX 79409-1021 USA (e-mail: beibei.ren@ttu.edu).

Color versions of one or more of the figures in this paper are available online at <http://ieeexplore.ieee.org>.

Digital Object Identifier 10.1109/TIE.2017.2740858

ples the dc/dc converter controller and the dc/ac converter controller, thus provides the dc bus voltage protection with enhanced fault ride-through performance on dc side, even in the fault conditions of the dc/ac converter or grid side. It is worth noting that the similar idea of the dc bus voltage regulated by generator side converter instead of grid side converter is already proposed for wind turbine control with the dc bus voltage protection [21], [22]. However, unlike the wind turbine control, MPPT function, particularly, perturbation-based MPPT algorithms, cannot be directly embedded with the power flow control of the dc/ac converter for grid-tied PV systems due to the low inertia of the PV system. An intermediate loop of PV voltage-regulation is proposed to build the linkage between MPPT function and power flow control for the dc/ac converter controller.

Furthermore, a new voltage dynamics is proposed for the dc/dc boost converter to avoid the nonminimum phase phenomenon existing in the nominal voltage dynamics. An uncertainty and disturbance estimator (UDE)-based current-mode controller (CMC) is proposed for the dc/dc boost converter, following the UDE design procedure [23] and the CMC design [24], [25]. The UDE-based method is adopted in both voltage-loop and current-loop to deal with model uncertainties, external disturbances, and estimation error of the inductor current to achieve the robust dc bus voltage regulation. For the dc/ac converter controller, inspired by the bounded integral controller in [20], a bounded-voltage power flow control strategy is proposed based on the existing UDE-based robust power flow control [26]. With the introduction of bounded-voltage design, the inverter output voltage always keeps within the given range. Hence, it can provide ac voltage protection in some fault modes, e.g., sensor errors, enhance the fault ride-through capability on ac side, and avoid the integrator windup caused by the saturation unit. Apart from the bounded-voltage power flow control, a gradient-based extremum seeking (ES) method [9], [27] is also adopted to achieve the MPPT. The PV voltage is regulated by a PI controller. The main contributions of this paper are highlighted as follows.

- 1) A new control structure is proposed for grid-tied PV systems where the dc bus voltage is regulated by the dc/dc converter controller, whereas the MPPT function and the power flow control are embedded into the dc/ac converter controller for dc bus voltage protection. An intermediate loop of PV voltage-regulation is designed to build the linkage between MPPT function and power flow control for the dc/ac converter controller.
- 2) A new voltage dynamics is developed for the dc/dc boost converter to avoid the nonminimum phase phenomenon existing in the nominal voltage dynamics. An UDE-based CMC is developed for the dc/dc boost converter with the robust dc bus voltage regulation.
- 3) A bounded-voltage power flow control strategy is proposed for the dc/ac converter to improve the existing UDE-based robust power flow control [26] for ac voltage protection.
- 4) The fault ride-through performance of the system is enhanced by both dc bus voltage protection and ac voltage protection.

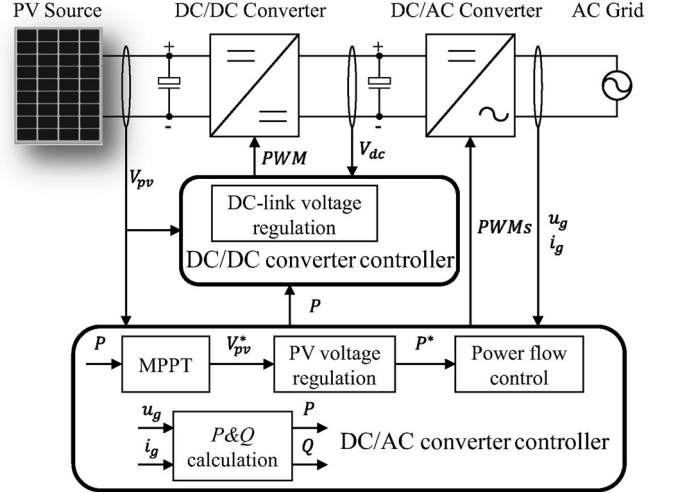


Fig. 1. System description of a grid-tied PV system with new control structure.

The effectiveness of the proposed control method is demonstrated through both experimental and simulation studies.

## II. SYSTEM DESCRIPTION AND MODELING

### A. System Description

A typical grid-tied PV system, as shown in Fig. 1, consists of a PV source, a dc/dc boost converter converting dc power with variable dc voltage of the PV source into a constant voltage dc bus, and a dc/ac converter feeding the dc power of the dc bus into an ac grid. Two dc bus capacitors  $C_{pv}$  and  $C_{dc}$  are used to smooth the output voltage of the PV source and the dc bus voltage, respectively.

In this paper, a new control structure for grid-tied PV systems will be investigated, which includes a dc/dc converter controller and a dc/ac converter controller as shown in Fig. 1. In the dc/dc converter controller, the dc bus voltage regulation is achieved, which converts dc power from PV source into the dc bus. The dc/ac converter controller includes a MPPT unit, a PV voltage-regulation unit, a bounded-voltage power flow control unit, and a power calculation unit to calculate system real power output  $P$  and reactive power output  $Q$  based on both output voltage  $u_g$  and output current  $i_g$ . The MPPT is used to maximize the system real power output  $P$ . The bounded-voltage power flow control converts the dc power from the dc bus to the ac grid with accurate power regulation. The PV voltage-regulation is designed to build the linkage between the MPPT function and the bounded-voltage power flow control.

Different from most existing works where the MPPT function is embedded into the dc/dc converter controller and dc bus voltage is regulated by the dc/ac converter controller, e.g., in [5]–[8], in this new control structure shown in Fig. 1, the MPPT function is embedded into the dc/ac converter controller, and the dc bus voltage is regulated by the dc/dc converter controller. In this way, the dc/dc converter controller and the dc/ac converter controller are decoupled. The dc bus voltage can always be regulated, even in the fault conditions from the dc/ac converter or

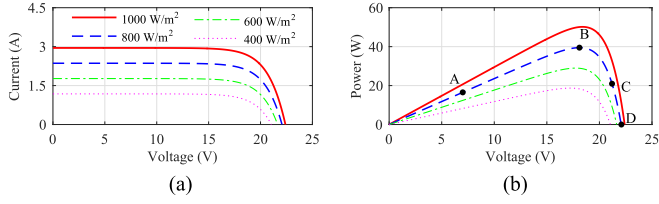


Fig. 2. Characteristics of PV source at  $T = 25^\circ\text{C}$  and different solar irradiation conditions. (a) Current–voltage curve. (b) Power–voltage curve.

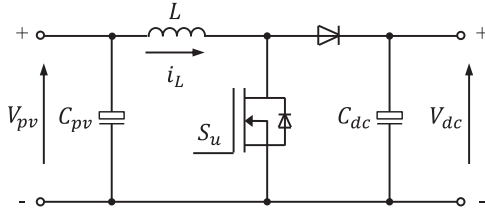


Fig. 3. DC/DC boost converter.

grid side, thus the fault ride-through performance on dc side is enhanced. The bounded-voltage power flow control can effectively regulate the inverter output voltage, which provides ac voltage protection and further improves the fault ride-through capability on ac side.

### B. Modeling of PV Source

A PV source/panel usually consists of several PV cells, and a popular five-parameter model for a PV cell can be found in [28] and [29]. According to this model, the fitting current–voltage and power–voltage curves for a solar panel, RENOGY RNG-50P [30], which is adopted for experimental validation in this paper, are shown in Fig. 2 at the temperature  $T = 25^\circ\text{C}$ .

### C. Modeling of DC/DC Boost Converter

Assume that the dc/dc boost converter shown in Fig. 3 supplies a load  $R_v$  representing the dc/ac converter, then its dynamics can be modeled as

$$\dot{V}_{dc} = -\frac{1}{R_v C_{dc}} V_{dc} + \frac{1}{C_{dc}} i_L - \frac{1}{C_{dc}} i_L u \quad (1)$$

$$\dot{i}_L = -\frac{1}{L} V_{dc} + \frac{1}{L} V_{dc} u + \frac{V_{pv}}{L} \quad (2)$$

where  $V_{pv}$  is the input voltage of the dc/dc boost converter, which is also the output voltage of the PV source,  $V_{dc}$  is the output voltage of the dc/dc converter, which is also the input voltage of the dc/ac converter,  $i_L$  is the inductor current and  $L$  is the inductance of the inductor, and  $u$  is the duty cycle of pulse width modulation (PWM) control signal  $S_u$  for power electronic device within the range of 0–100%. For this dc/dc boost converter, the averaged relationship between the input voltage  $V_{pv}$  and output voltage  $V_{dc}$  is given as  $V_{dc} = \frac{V_{pv}}{1-u}$ , which indicates the output voltage  $V_{dc}$  has a positive correlation with the system input  $u$ . However, the term  $-\frac{1}{C_{dc}} i_L u$  in voltage dynamics (1) has an inverse response with  $\frac{1}{C_{dc}} i_L > 0$ . This is also called the nonminimum phase phenomenon [24], [31]. So,

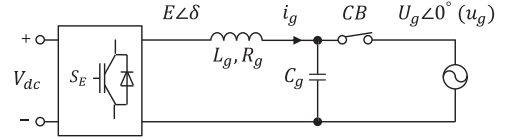


Fig. 4. DC/AC converter.

the voltage dynamics (1) is usually not directly used for the controller design, and even omitted.

### D. Modeling of DC/AC Converter

The equations of power delivery from the dc/ac converter to the grid, shown in Fig. 4, can be obtained as [1]

$$P = \left( \frac{EU_g}{Z} \cos \delta - \frac{U_g^2}{Z} \right) \cos \theta + \frac{EU_g}{Z} \sin \delta \sin \theta \quad (3)$$

$$Q = \left( \frac{EU_g}{Z} \cos \delta - \frac{U_g^2}{Z} \right) \sin \theta - \frac{EU_g}{Z} \sin \delta \cos \theta \quad (4)$$

where  $\delta$  is the phase lead between output voltage of inverter bridge  $E\angle\delta$  and ac grid  $U_g\angle 0^\circ$ , often called the power angle. The grid voltage  $u_g$  is used as the reference, so its initial angle is defined as zero. The output impedance  $Z\angle\theta$  is defined as  $Z\angle\theta = R_g + X_g j$ , where  $X_g j$  is mostly dominated by  $L_g$ , as the output capacitor  $C_g$  is usually very small.

Following the procedures of obtaining the dynamics of power delivering in [26], taking derivatives of both (3) and (4) results in

$$\dot{P} = \frac{EU_g}{Z} \dot{\delta} + \Delta_p \quad (5)$$

$$\dot{Q} = \frac{U_g}{Z} \dot{E} + \Delta_q \quad (6)$$

where

$$\Delta_p = \frac{EU_g \dot{\delta}}{Z} (\cos \delta \sin \theta - 1) - \frac{EU_g \dot{\delta}}{Z} \sin \delta \cos \theta$$

$$+ \frac{U_g \dot{E}}{Z} \cos \delta \cos \theta + \frac{U_g \dot{E}}{Z} \sin \delta \sin \theta$$

$$\Delta_q = \frac{U_g \dot{E}}{Z} (\cos \delta \sin \theta - 1) - \frac{U_g \dot{E}}{Z} \sin \delta \sin \theta$$

$$- \frac{EU_g \dot{\delta}}{Z} \cos \delta \cos \theta - \frac{U_g \dot{E}}{Z} \sin \delta \cos \theta$$

represent the lumped uncertain terms, including the uncertainties, the nonlinearity, and the coupling effects of power angle  $\delta$  and output impedance  $Z\angle\theta$ .

## III. DC/DC CONVERTER CONTROLLER DESIGN

In this section, the dc/dc converter controller with a dc bus voltage regulation module, shown in Fig. 1, will be designed. Because the inverse response or the nonminimum phase phenomenon exist in the voltage dynamics of the dc/dc boost converter, the voltage dynamics is redesigned to avoid this phenomenon. Following the UDE procedure [23] and the CMC

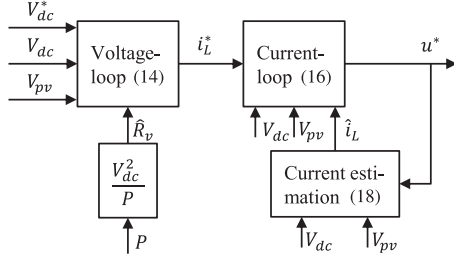


Fig. 5. Cascaded control scheme for the dc/dc converter controller.

design [24], [25], an UDE-based CMC is developed for the dc/dc boost converter in grid-tied PV systems, as shown in Fig. 5. Also, an inductor current estimation is adopted to avoid the usage of current sensor.

### A. Revised Dynamics of DC/DC Boost Converter

By setting  $\dot{V}_{dc} = 0$  in (1) and  $\dot{i}_L = 0$  in (2), a power balance equation at steady state can be obtained as

$$V_{dc}^2 = V_{pv} R_v i_L \quad (7)$$

where the input power  $V_{pv} i_L$  is equal to the output power  $\frac{V_{dc}^2}{R_v}$  without considering the losses of components and parasitics.

In practice, in order to filter the switching harmonics and other high-frequency noises, a low-pass filter is commonly adopted for voltage measurement. Following the similar method in [32] with the choice of a first-order low-pass filter  $G_{sv} = \frac{1}{1 + \tau_{sv} s}$ , where  $\tau_{sv}$  is the time constant, the power balance equation (7) can be rewritten as

$$V_{dc}^2 = L^{-1} \left\{ \frac{1}{1 + \tau_{sv} s} \right\} * (V_{pv} R_v i_L)$$

where “\*” is the convolution operator, and  $L^{-1}$  means the inverse Laplace transformation. Then

$$\dot{V}_{dc} = \frac{V_{pv} R_v}{2\tau_{sv} V_{dc}} i_L - \frac{V_{dc}}{2\tau_{sv}}. \quad (8)$$

Considering the losses of components and parasitics in both voltage dynamics (8) and current dynamics (2), the revised dynamics of the dc/dc boost converter can be rewritten as

$$\dot{V}_{dc} = \frac{V_{pv} R_v}{2\tau_{sv} V_{dc}} i_L - \frac{V_{dc}}{2\tau_{sv}} + \Delta_v \quad (9)$$

$$\dot{i}_L = -\frac{1}{L} V_{dc} + \frac{1}{L} V_{dc} u + \frac{V_{pv}}{L} + \Delta_i \quad (10)$$

where  $\Delta_v$  and  $\Delta_i$  represent the uncertain terms, which include the model uncertainties (e.g., the parasitics), and the effects of the losses of components.

### B. Controller Design

In this section, the UDE-based method embedded in the backstepping design framework [33] is adopted for the cascaded voltage-loop and current-loop control designs to deal with model uncertainties, external disturbances, and estimation error of the inductor current.

**1) Voltage-Loop Design:** The control objective is to design a virtual control input  $i_L^*$  to make the output voltage  $V_{dc}$  asymptotically track the voltage reference  $V_{dc}^*$ , as shown in Fig. 5. The tracking error,  $e_v = V_{dc}^* - V_{dc}$ , should satisfy the error dynamic equation

$$\dot{e}_v = -k_v e_v \quad (11)$$

where  $k_v > 0$  is a constant error feedback gain. Combining (9) and (11),  $i_L^*$  needs to satisfy

$$i_L^* = \frac{2\tau_{sv} V_{dc}}{V_{pv} R_v} \left( \dot{V}_{dc}^* + \frac{V_{dc}}{2\tau_{sv}} - \Delta_v + k_v e_v \right). \quad (12)$$

According to the voltage dynamics (9), the uncertainty term  $\Delta_v$  can be represented as  $\Delta_v = \dot{V}_{dc} - \frac{V_{pv} R_v}{2\tau_{sv} V_{dc}} i_L^* + \frac{V_{dc}}{2\tau_{sv}}$ . Following the procedures in [23],  $\Delta_v$  can be estimated by

$$\begin{aligned} \hat{\Delta}_v &= L^{-1} \{G_{vf}(s)\} * \Delta_v \\ &= L^{-1} \{G_{vf}(s)\} * \left( \dot{V}_{dc} - \frac{V_{pv} R_v}{2\tau_{sv} V_{dc}} i_L^* + \frac{V_{dc}}{2\tau_{sv}} \right) \end{aligned} \quad (13)$$

where  $G_{vf}(s)$  is a strictly proper stable filter with the appropriate bandwidth to cover the spectrum of  $\Delta_v$ . Replacing  $\Delta_v$  with  $\hat{\Delta}_v$  in (12), results in the UDE-based control law

$$\begin{aligned} i_L^* &= \frac{V_{dc}^2}{V_{pv} R_v} - \frac{2\tau_{sv} V_{dc}}{V_{pv} R_v} \left[ L^{-1} \left\{ \frac{s G_{vf}(s)}{1 - G_{vf}(s)} \right\} * V_{dc} \right. \\ &\quad \left. - L^{-1} \left\{ \frac{1}{1 - G_{vf}(s)} \right\} * (\dot{V}_{dc}^* + k_v e_v) \right]. \end{aligned} \quad (14)$$

Here, the load of the dc/dc converter  $R_v$  appears in the denominator in (14), which can be calculated as,  $R_v = \frac{V_{dc}^2}{P_{dc}}$ , where  $P_{dc}$  is the output power of the dc/dc converter. When  $P_{dc}$  is not measured in some cases, e.g., the experimental hardware limitation in this paper, the output power of dc/ac converter  $P$  can be used to approximately estimate  $R_v$ , i.e.,  $\hat{R}_v = \frac{V_{dc}^2}{P}$ . However, the deviation between  $R_v$  and  $\hat{R}_v$  can be lumped into the uncertain term  $\Delta_v$  and handled by this UDE-based control law (14). When  $P$  is zero, it can be replaced with a small positive number.

**2) Current-Loop Design:** With  $i_L^*$  designed in the Section III-B1, the control objective in this section is to manipulate the duty cycle  $u^*$ , such that the inductor current  $i_L$  tracks the reference signal  $i_L^*$ , as shown in Fig. 5. The tracking error  $e_i = i_L^* - i_L$  still needs to satisfy

$$\dot{e}_i = -k_i e_i \quad (15)$$

where  $k_i > 0$  is a constant error feedback gain. Combining (10) and (15), and following the similar procedures in the previous section, the UDE-based control law for the duty cycle  $u^*$  can be obtained as

$$\begin{aligned} u^* &= 1 - \frac{V_{pv}}{V_{dc}} - \frac{L}{V_{dc}} \left[ L^{-1} \left\{ \frac{s G_{if}(s)}{1 - G_{if}(s)} \right\} * i_L \right. \\ &\quad \left. - L^{-1} \left\{ \frac{1}{1 - G_{if}(s)} \right\} * (i_L^* + k_i e_i) \right] \end{aligned} \quad (16)$$

where  $G_{if}(s)$  is a strictly proper stable filter with the appropriate bandwidth to cover the spectrum of uncertain term  $\Delta_i$ .

It is worth noting that the UDE-based control laws (14) and (16) include the derivative terms  $\dot{V}_{dc}^*$  and  $\dot{i}_L^*$ , which can be numerically approximated using the low pass filters [32].

### C. Estimation of Inductor Current

In order to reduce system cost and provide system reliability, the current estimation  $\hat{i}_L$  is usually adopted instead of direct measurement of inductor current  $i_L$  for the current-loop design. To guarantee the convergence of the current estimation error, the original current dynamics (10) is revised with an additional term  $-\frac{R_L}{L}i_L$  from the inductor parasitics, with  $\frac{R_L}{L}i_L = \Delta'_i - \Delta_i$ , then

$$\dot{i}_L = -\frac{1}{L}V_{dc} + \frac{1}{L}V_{dc}u^* + \frac{V_{pv}}{L} - \frac{R_L}{L}i_L + \Delta'_i \quad (17)$$

where  $R_L$  is the parasitics resistance and its nominal value can be measured easily. With the known input voltage  $V_{pv}$ , output voltage  $V_{dc}$  and the duty cycle  $u^*$ , the current estimation law is designed as

$$\dot{\hat{i}}_L = -\frac{1}{L}V_{dc} + \frac{1}{L}V_{dc}u^* + \frac{V_{pv}}{L} - \frac{R_L}{L}\hat{i}_L. \quad (18)$$

The discrete form of this current estimation law can be found in [34] and [35].

Defining the estimation error  $e_{oi} = i_L - \hat{i}_L$ , the error dynamics of the current estimation is obtained as

$$\dot{e}_{oi} = -\frac{R_L}{L}e_{oi} + \Delta'_i. \quad (19)$$

Solving (19) results in

$$e_{oi}(t) = e_{oi}(0)e^{-ct} + \frac{\Delta'_i}{c}(1 - e^{-ct})$$

where  $c = \frac{R_L}{L} > 0$ , and  $e_{oi}(0)$  is the initial error. When  $t \rightarrow \infty$ , the estimation error  $e_{oi}(t)$  is bounded by  $\frac{\Delta'_i}{c}$ , in other words,  $|e_{oi}(\infty)| < \frac{\max_t |\Delta'_i|}{c}$ . Usually, this bound  $\frac{\max_t |\Delta'_i|}{c}$  is small, as  $\Delta'_i$  is small and  $c$  is large in practice. In this cascaded control system, as shown in Fig. 5, the error in current estimation will be propagated to the calculation of the current reference  $i_L^*$  in steady state. However, the bounded error in  $i_L^*$  can be lumped into the uncertain term  $\Delta_v$ , and compensated by the UDE-based controller (14) in the voltage-loop, thus the good voltage tracking performance still can be achieved. This feature will be experimentally demonstrated in Section V.

## IV. DC/AC CONVERTER CONTROLLER DESIGN

As shown in Fig. 1, the dc/ac converter controller includes three cascaded control modules: the MPPT, the PV voltage-regulation, and the bounded-voltage power flow control. The detailed control structure are shown in Fig. 6.

### A. MPPT

The output power of the PV source is affected by the output voltage  $V_{pv}$  given a constant solar irradiation level, as shown in Fig. 2. In order to maximize the system real power output  $P$ , the gradient-based ES algorithm [9], [27] is introduced to estimate

its gradient by injecting a small perturbation,  $a\sin(\omega_0 t)$ , on the reference voltage of PV source  $V_{pv}^*$ , as shown in Fig. 6. It is required that the ES algorithm should work more slowly than the whole PV system dynamics. A high-pass filter  $\frac{s}{s+\omega_h}$  filters the dc part of  $P$ . The multiplication of the resulting signal  $P - \bar{P}$  by  $\sin(\omega_0 t)$  creates an estimation of the gradient of  $P$ , which is smoothed by a low-pass filter  $\frac{\omega_l}{s+\omega_l}$ . When  $V_{pv}$  is smaller (larger) than its optimal value, the estimation of the gradient  $\hat{g}$  is positive (negative) and  $V_{pv}^*$  increases (decreases), which drives  $V_{pv}$  toward its optimal value. Thus, the maximum power output  $P$  can be achieved.  $k_{es} > 0$  is a constant integral gain for  $\hat{g}$ .

### B. PV Voltage-Regulation

In order to regulate the output voltage of PV source  $V_{pv}$  to its reference  $V_{pv}^*$  for MPPT, as shown in Fig. 6, a PI controller is introduced to generate the real power reference  $P^*$

$$P^* = -K_{ppv}(V_{pv}^* - V_{pv}) - K_{ipv} \int (V_{pv}^* - V_{pv}) dt \quad (20)$$

where,  $K_{ppv} > 0$  and  $K_{ipv} > 0$  are proportional gain and integral gain, respectively.

### C. Bounded-Voltage Power Flow Control

In [26], an UDE-based robust power flow controller was proposed based on the dynamics of power delivering dynamics (5) and (6) for the dc/ac inverter, which is described by

$$\dot{\delta} = \frac{Z}{EU_g} \left[ L^{-1} \left\{ \frac{1}{1 - G_{pf}(s)} \right\} * (\dot{P}^* + k_p e_p) - L^{-1} \left\{ \frac{sG_{pf}(s)}{1 - G_{pf}(s)} \right\} * P \right] \quad (21)$$

$$\dot{E} = \frac{Z}{U_g} \left[ L^{-1} \left\{ \frac{1}{1 - G_{qf}(s)} \right\} * (\dot{Q}^* + k_q e_q) - L^{-1} \left\{ \frac{sG_{qf}(s)}{1 - G_{qf}(s)} \right\} * Q \right] \quad (22)$$

where  $P^*$  is the real power reference from the PV voltage-regulation loop,  $Q^*$  is the reactive power reference;  $e_p = P^* - P$ , and  $e_q = Q^* - Q$  are power tracking errors;  $k_p > 0$  and  $k_q > 0$  are constant error feedback gains to achieve the error dynamics  $\dot{e}_p = -k_p e_p$ , and  $\dot{e}_q = -k_q e_q$ . The UDE filters  $G_{pf}(s)$  and  $G_{qf}(s)$  are strictly-proper stable filters with the appropriate bandwidth for the estimation of the uncertain terms  $\Delta_p$  in (5) and  $\Delta_q$  in (6). Though the robustness of the UDE-based robust power flow controller is achieved in [26] in the presence of model uncertainties and external disturbances, how to guarantee the bounded output voltage of the inverter with ac voltage protection has not been considered yet.

In this paper, an improved bounded-voltage power flow control, as shown in Fig. 6, will be redesigned to maintain the inverter output voltage within the range of  $[-E_{max}, E_{max}]$ . Following the concept of bounded integral controller in [18] and [20], the voltage regulation (22) is modified by adding a

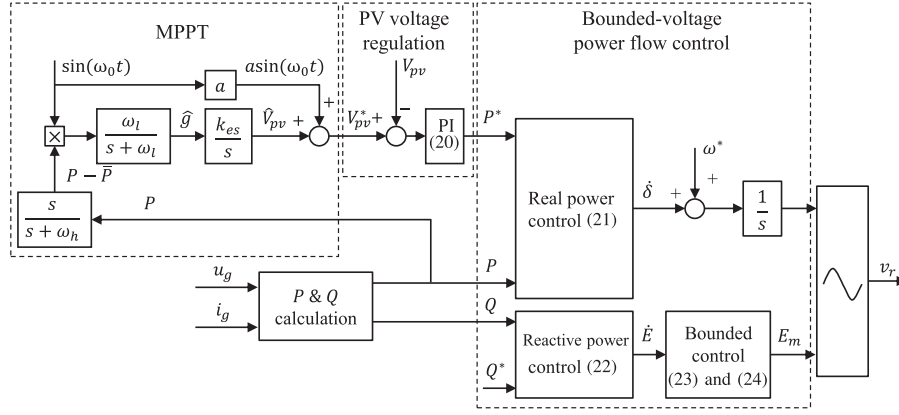


Fig. 6. Control scheme for the dc/ac converter controller.

bounded-voltage controller

$$\dot{E}_m = -k \left( \frac{E_m^2}{E_{\max}^2} + E_q^2 - 1 \right) E_m + E_q^2 \dot{E} \quad (23)$$

$$\dot{E}_q = -k \left( \frac{E_m^2}{E_{\max}^2} + E_q^2 - 1 \right) E_q - \frac{E_q E_m}{E_{\max}^2} \dot{E} \quad (24)$$

where  $E_m$  is the modified voltage regulation output,  $E_q$  is an additional variable with the initial states  $E_{m0} = E^*$ ,  $E_{q0} = \sqrt{1 - \frac{(E^*)^2}{E_{\max}^2}}$ ,  $E^*$  is the nominal grid voltage, and  $k > 0$  is a positive constant gain.

Considering the following Lyapunov function candidate

$$V_E(t) = \frac{E_m^2}{E_{\max}^2} + E_q^2.$$

Taking the derivative of  $V_E(t)$  along with (23) and (24), there is

$$\dot{V}_E(t) = -2kV_E^2(t) + 2kV_E(t). \quad (25)$$

Then, solving (25) gives

$$\begin{aligned} V_E(t) &= \frac{e^{2kt} V_E(0)}{e^{2kt} V_E(0) - V_E(0) + 1} \\ &= \frac{1}{1 - e^{-2kt} \left(1 - \frac{1}{V_E(0)}\right)}. \end{aligned} \quad (26)$$

Given the initial conditions  $E_{m0} = E^*$ ,  $E_{q0} = \sqrt{1 - \frac{(E^*)^2}{E_{\max}^2}}$ , there is

$$V_E(0) = 1 \Rightarrow V_E(t) = 1 \quad \forall t \geq 0.$$

If there are any parametric errors in  $V_E(0)$ ,  $V_E(t)$  will still converge to one with  $e^{-2kt} \left(1 - \frac{1}{V_E(0)}\right) \rightarrow 0$ , when  $t \rightarrow \infty$ . So

$$\frac{E_m^2}{E_{\max}^2} + E_q^2 = 1$$

which indicates that  $E_m$  is always bounded in the given range  $E_m \in \{-E_{\max} < E_m < E_{\max}\}$ , and  $E_q \in \{0 < E_q \leq 1\}$ , no matter how  $\dot{E}$  changes. In practice,  $E_m$  should be greater than zero. In the steady state,  $\dot{E}$ ,  $\dot{E}_m$ , and  $\dot{E}_q$  will be regulated to zero, then both controller states  $E_m$  and  $E_q$  will converge to the equilibrium point  $(E_{me}, E_{qe})$ , as shown in Fig. 7.

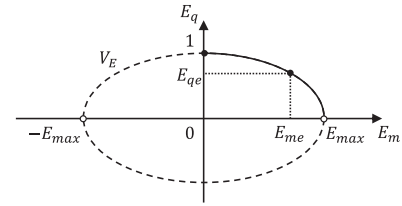


Fig. 7. Phase portrait of the voltage dynamics in the bounded-voltage controller (23) and (24).

#### D. Need of PV Voltage-Regulation Loop

Among the three cascaded loops of the dc/ac converter controller in Fig. 6, the inner loop, bounded-voltage power flow control, is much faster than the outer loop, MPPT. In this section, the need of the intermediate loop, PV voltage-regulation, will be discussed especially when the system operates at its maximum power point. The condition when the solar irradiation is equal to  $800 \text{ W/m}^2$ , as shown in Fig. 2(b), is taken as an example. The system is assumed to operate at its maximum power point, e.g., point B, with the corresponding PV voltage  $V_B$  and maximum power output  $P_B$ . Even if a perturbation signal  $\Delta V = a \sin(\omega_0 t)$  from MPPT is added to  $V_B$ , the PV voltage-regulation loop, together with the fast response of the bounded-voltage power flow control, can stabilize the PV voltage within the range  $[V_B - a, V_B + a]$  and guarantee the system operates near to point B. However, without the PV voltage-regulation loop, the perturbation-based MPPT will be applied to the power flow control directly. The perturbation signal from MPPT  $\Delta P = a' \sin(\omega_0' t)$  is added to the maximum power  $P_B$  directly. When  $\Delta P > 0$ , the power output of PV source will be overloaded, which will cause the system to operate from point B to point A, or even unstable. This can be explained as follows: the slow response of MPPT cannot compensate this fast overload of the power output in PV source; and the PV source does not have any inertia to support the extra power output, which is different from the wind turbine systems. Therefore, the intermediate loop, PV voltage-regulation, is essential in the proposed control structure, as shown in Figs. 1 and 6.

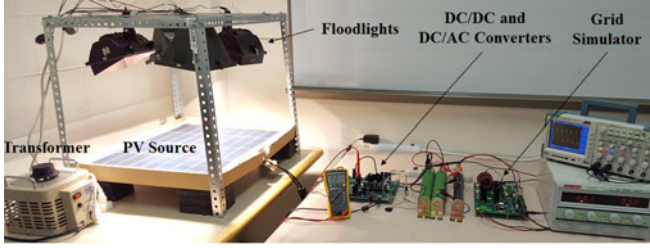


Fig. 8. Experimental setup.

TABLE I  
SYSTEM PARAMETERS

Parameters	Values	Parameters	Values
$C_{pv}$	680 $\mu\text{F}$	$L_g$	200 $\mu\text{H}$
$L$	100 $\mu\text{H}$	$R_g$	0.4 $\Omega$
$R_L$	0.2 $\Omega$	$C_g$	3 $\mu\text{F}$
$C_{dc}$	1640 $\mu\text{F}$	Nominal grid voltage $E^*$	20 $\text{V}_{\text{rms}}$
$V_{dc}^*$	35 V	Nominal grid frequency $\omega^*$	120 $\pi$ rad/s

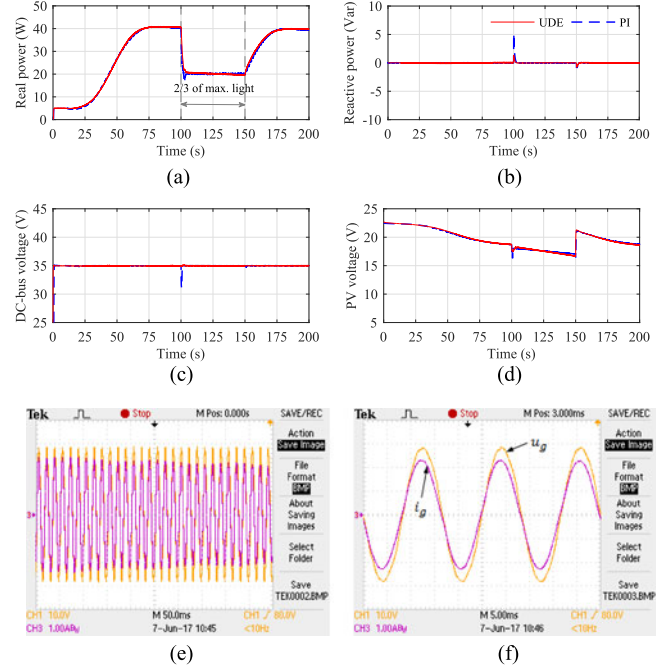
TABLE II  
CONTROL PARAMETERS

Parameters	Values	Parameters	Values	Parameters	Values
$\tau_{sv}$	0.001 s	$\omega_0$	10 $\pi$ rad/s	$k_p, k_q$	20
$k_v$	10	$a$	0.25	$G_{pf}(s)$	$\frac{1}{1+\tau_p s}$
$k_i$	100	$k_{es}$	0.2	$G_{pf}(s)$	$\frac{1}{1+\tau_q s}$
$G_{vf}(s)$	$\frac{1}{1+\tau_v s}$	$\omega_h$	2 $\pi$ rad/s	$\tau_p$	0.005
$G_{if}(s)$	$\frac{1}{1+\tau_i s}$	$\omega_l$	5 $\pi$ rad/s	$\tau_q$	0.005
$\tau_v$	0.01 s	$K_{ppv}$	1	$E_{\text{max}}$	1.1 $E^*$
$\tau_i$	0.001 s	$K_{ipv}$	5	$k$	1000

## V. EXPERIMENTAL RESULTS

### A. Experimental Setup

To verify the proposed new control structure of grid-tied PV systems, a lab-environment test rig with one PV system delivering power to a grid simulator, is built as shown in Fig. 8, wherein the PV system includes a solar panel RENOGY RNG-50P, a Texas Instruments (TI) solar explorer kit consisting of a dc/dc boost converter and a single-phase dc/ac converter, and four 450 W halogen floodlights which can be tuned by a transformer to mimic the sunlight. The grid simulator [26] consists of a controlled inverter powered by a dc source and a 9  $\Omega$  resistor load. The system parameters are listed in Table I. The control parameters for both dc/dc converter controller and dc/ac converter controller are provided in Table II. How to choose parameters in UDE-based controllers can refer to [23], [26], [36]. The parameters design in the PV voltage-regulation controller (20) can refer to the slope on the right hand side of the PV power–voltage curve, e.g., the B-C-D in Fig. 2(b), as the PV source usually operates from point D to point B with MPPT control. However, the PV source works at different solar irradiation

Fig. 9. Experimental results for change of sunlight (Case 1). (a) Real power output  $P$ . (b) Reactive power output  $Q$ . (c) DC bus voltage. (d) PV output voltage. (e) Transient voltage  $u_g$  and current  $i_g$ . (f) Transient  $u_g$  and  $i_g$  (zoom in).

conditions. The nominal values of these parameters,  $K_{ppv}$ ,  $K_{ipv}$ , can be chosen based on the power–voltage curve at the low solar irradiation, then further tuned to satisfy the power oscillations at the maximum power point are small, and the PV voltage-regulation loop is fast enough to fulfill the requirement of the MPPT algorithm. The PWM frequencies for the dc/dc converter and dc/ac converter are 100 kHz and 20 kHz, respectively.

### B. System Performance

1) **Case 1: Change of Sunlight:** To test the performance of maximum power acquisition in nominal operation of the grid-tied PV system with the proposed new control structure in Fig. 1, the change of sunlight is considered. At  $t = 0$  s, the floodlights are set at their maximum outputs, and the dc/dc boost converter starts to regulate the dc bus voltage. Then, the dc/ac converter delivers a small amount of power to the simulated grid (5 W setting), and the MPPT is enabled at  $t = 10$  s. At  $t = 100$  s, the floodlights are set at about 2/3 of their maximum output, and back to the maximum at  $t = 150$  s.

The system responses are shown in Fig. 9. Initially, the dc bus voltage in Fig. 9(c) is regulated to the set-point 35 V. After enabling MPPT, the real power output  $P$  in Fig. 9(a) goes up to the maximum value within 60 s, and the PV output voltage in Fig. 9(d) drops correspondingly. After  $t = 100$  s, the real power output drops quickly with 2/3 of the maximum output of floodlights. The PV output voltage has a small drop. The corresponding transient voltage  $u_g$  and current  $i_g$  captured from the oscilloscope are shown in both Fig. 9(e) and (f). At  $t = 150$  s, the PV output voltage goes up, as the floodlights are given at their maximum output. The real power output achieves the maximum

value again within 30 s. The system with the proposed new control structure demonstrates a good performance of maximum power acquisition within different sunlight conditions. The reactive power output in Fig. 9(b) almost keeps 0 Var through the whole experimental test. The proposed method can achieve good power regulation. It can be seen that the dc bus voltage always keeps at the set-point value during the whole experiment. So, the proposed UDE-based CMC has good performance of the dc bus voltage regulation in the presence of the model uncertainties (e.g., parasitics), the external disturbances (e.g., load change caused by the change of sunlight), and current estimation error. It is worth noting that both the real power output and PV output voltage drop slowly during the steady states. The reason is that the temperature of solar panel increases slowly with high irradiation of the floodlights.

To further show the advantages of the UDE-based controllers, three PI controllers are introduced in same control structure to replace the UDE-based controllers. For fair comparison, the parameters of PI controllers are chosen with similar transient- and steady-state performance to the UDE-based controllers for the nominal case (without uncertainties and disturbances). In particular, the PI controller for the dc bus voltage regulation is designed as

$$u^* = K_{pdc}(V_{dc}^* - V_{dc}) + K_{idc} \int (V_{dc}^* - V_{dc}) dt$$

with  $K_{pdc} = 0.1$ ,  $K_{idc} = 0.5$ . The design of PI controllers for bounded-voltage power flow control can refer to [26], where the parameters are chosen as  $k_{pp} = 0.11$  and  $k_{ip} = 0.94$  for real power channel,  $k_{pq} = 2.22$  and  $k_{iq} = 18.32$  for reactive power channel.

The comparison results are shown in Fig. 9. It can be seen that the PI controllers have similar transient- and steady-state performance to the UDE-based controllers before  $t = 100$  s. However, the PI controllers have a large spike in the dc bus voltage, when floodlights are quickly changed to a low level at  $t = 100$  s. Accordingly, the system also has some transient spikes in the real power output  $P$ , reactive power output  $Q$ , and PV output voltage at  $t = 100$  s. After the transient periods, the PI controllers hold the similar performance to the UDE-based controllers again. Therefore, the UDE-based controllers have better robustness than the PI controllers to handle uncertainties and disturbances in this grid-tied solar system.

**2) Case 2: Fault Ride-Through With AC Grid Fault:** To further evaluate the fault ride-through performance of the proposed new control structure on dc side, an ac grid fault is considered. The floodlights are given at their maximum output. With the same initial setting of Case 1, MPPT is enabled after  $t = 10$  s. At  $t = 100$  s, the dc/ac inverter is turned OFF to simulate an ac grid fault, and is turned ON at  $t = 120$  s.

The system responses are shown in Fig. 10. The system goes to its maximum real power output at  $t = 75$  s. At  $t = 100$  s, both real power and reactive power are zero, as shown in Fig. 10(a) and (b), respectively, because the fault is simulated at ac grid. The dc bus voltage in Fig. 10(c) increases by 16.6% quickly, because the dc/ac converter is OFF. However, the proposed control structure can still regulate the dc bus voltage to 35 V without

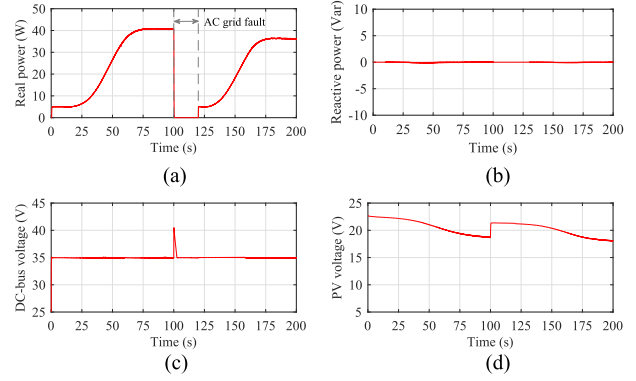


Fig. 10. Experimental results for ac grid fault (Case 2). (a) Real power output  $P$ . (b) Reactive power output  $Q$ . (c) DC bus voltage. (d) PV output voltage.

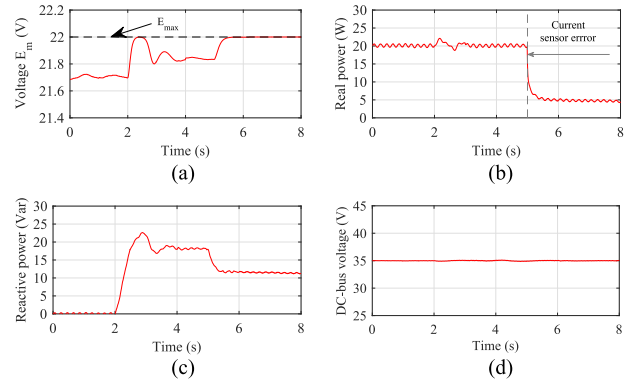


Fig. 11. Experimental results for current sensor error (Case 3). (a) Voltage  $E_m$ . (b) Real power output  $P$ . (c) Reactive power output  $Q$ . (d) DC bus voltage.

any dc bus voltage protection units. It is worth noting that the energy in dc bus capacitor can be consumed by a sampling resistance (10 k $\Omega$  is used in the experiment), though the dc/ac converter is switched OFF. The PV output voltage in Fig. 10(d) goes up accordingly without any power output. When the fault is cleared at  $t = 120$  s, a small amount of power is delivered to the grid simulator (5 W setting), then MPPT is enabled, and the system is back to its maximum output again within 60 s. The proposed method can regulate the dc bus voltage well, even in the fault condition of grid side without a protection unit. Also, the proposed method has a good fault-ride through capability with ac grid fault.

**3) Case 3: Fault Ride-Through With AC Current Sensor Error:** To test the fault ride-through performance of the proposed bounded-voltage power flow control on ac side, a current sensor fault is considered. The grid voltage is set at 21 V<sub>rms</sub>. The floodlights are given at about 2/3 of their maximum output. Initially, the system already operates at its MPPT condition. At  $t = 2$  s, the reactive power reference is set at  $Q^* = 20$  var. At  $t = 5$  s, the ac current sensor fault is injected as the measured value is only 25% of its actual value.

The system responses are shown in Fig. 11. The real power output is about 20 W, because of 2/3 of maximum output of floodlights, as shown in Fig. 11(b). After the reactive power is

TABLE III  
SYSTEM PARAMETERS

Parameters	Values	Parameters	Values
$C_{pv}$	1000 $\mu$ F	$V_{dc}^*$	400 V
$L$	100 $\mu$ H	$L_g$	2.2 mH
$R_L$	0.1 $\Omega$	$R_g$	0.5 $\Omega$
$C_{dc}$	2000 $\mu$ F	$C_g$	10 $\mu$ F

TABLE IV  
CONTROL PARAMETERS

Parameters	Values	Parameters	Values	Parameters	Values
$\omega_0$	10 $\pi$ rad/s	$\omega_h$	2 $\pi$ rad/s	$K_{ipv}$	100
$a$	2.5	$\omega_l$	5 $\pi$ rad/s	$E_{max}$	1.2 $E^*$
$k_{es}$	0.5	$K_{ppv}$	20	$k$	1000

set to 20 var at  $t = 2$  s, the proposed bounded-voltage control regulates the output voltage  $E_m$  inside the given bounded range within  $E_{max}$  (22 V<sub>rms</sub>), as shown in Fig. 11(a). Then, the reactive power reaches the setting point with some oscillations, as shown in Fig. 11(c). After  $t = 5$  s, the current sensor fault is injected. The calculated real power goes to about 5 W, however, the actual real power is about 20 W. The output voltage  $E_m$  reaches its maximum value  $E_{max}$  with more reactive power delivered to the grid, because of the current sensor error. Though the calculated reactive power is about 12 var, the actual value should be about 48 var. Hence, the proposed bounded-voltage control can regulate the voltage  $E_m$  within the given range to realize ac voltage protection. The dc bus voltage in Fig. 11(d) is still well regulated, as the actual real power is used for  $\hat{R}_v$  estimation. It can be seen that the system has a good fault ride-through performance when the ac current sensor fault occurs.

## VI. SIMULATION STUDIES

To further demonstrate the need of the intermediate PV voltage-regulation loop and the merits of the proposed bounded-voltage power flow control, a simulation platform with the same structure in Fig. 1 is built in MATLAB/Simulink/SimPower Systems to study more realistic scales. The PV source is considered as a  $10 \times 10$  series-parallel array of solar panels, RENOGY RNG-50P, and the dc/ac converter is connected to a three-phase ac grid with rated phase voltage of 110 V<sub>rms</sub> and 60 Hz. The system parameters are shown in Table III, and the control parameters for MPPT and PV voltage-regulation are redesigned in Table IV. It is worth noting that there is no need to redesign the parameters for the UDE-based controllers due to their good robustness, even if the system scale is changed.

### A. Case 4: With/Without PV Voltage-Regulation Loop

To test the need of PV voltage-regulation loop, two controllers with/without PV voltage-regulation loop are compared. In the controller without PV voltage-regulation loop, the

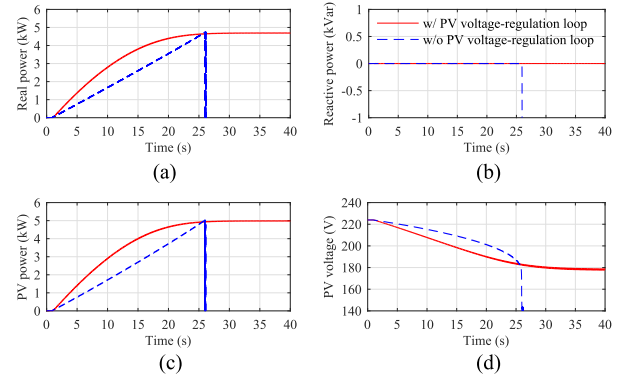


Fig. 12. Simulation results with/without PV voltage-regulation loop (Case 4). (a) Real power output  $P$ . (b) Reactive power output  $Q$ . (c) PV output power  $P_{pv}$ . (d) PV output voltage.

perturbation signal from MPPT is added to  $P^*$  directly. The maximizing target is chosen as the PV output power  $P_{pv}$ , because the perturbation signal and maximizing target cannot be the same variable in ES algorithm. For fair comparison, the PV output power  $P_{pv}$  is the maximizing target in the controller with PV voltage-regulation loop too. The perturbation gain  $a' = 25$  and integral gain  $k'_{es} = 20$  are chosen in ES algorithm for the controller without PV voltage-regulation loop, while  $a = 2.5$  and  $k_{es} = 0.5$  are selected for the controller with PV voltage-regulation loop to make two controllers have similar MPPT convergence time. The system starts at  $t = 0$  s. The sunlight is considered as 1000 W/m<sup>2</sup>. With the same initial settings as Case 1, the MPPT is enabled after  $t = 1$  s, and the system stops at  $t = 40$  s.

The system responses are shown in Fig. 12. After enabling MPPT, the real power output  $P$  in Fig. 12(a) goes up to the maximum point within about 26 s in both controllers. In the controller with PV voltage-regulation loop,  $P$  increases with a nonlinear behavior, as the perturbation signal  $V_{pv}^*$  has a nonlinear relationship with the maximizing target  $P_{pv}$ , as shown in Fig. 2(b). However, in the controller without PV voltage-regulation loop,  $P$  increases linearly, as the perturbation signal  $P^*$  has an approximately linear relationship with  $P_{pv}$ . The PV output power  $P_{pv}$  in Fig. 12(c) has a similar shape to  $P$ , but is slightly higher than  $P$  in both controllers, because of power losses. After about 27 s, the controller with the PV voltage-regulation loop converges to its steady state with the maximum power output. However, the controller without the PV voltage-regulation loop becomes unstable with large drops and oscillations in both the real power output and PV power output, whereas the PV output voltage and reactive power output drop dramatically, as shown in Fig. 12(d) and (b), respectively. This is because the PV source is overloaded at its maximum point, as discussed in Section IV-D.

### B. Case 5: Comparison With the Saturation Unit

To further demonstrate the advantage of the proposed bounded-voltage power flow control, its performance is compared with the existing UDE-based robust power flow control [26] by adding a saturation unit. The system starts at  $t = 0$  s.

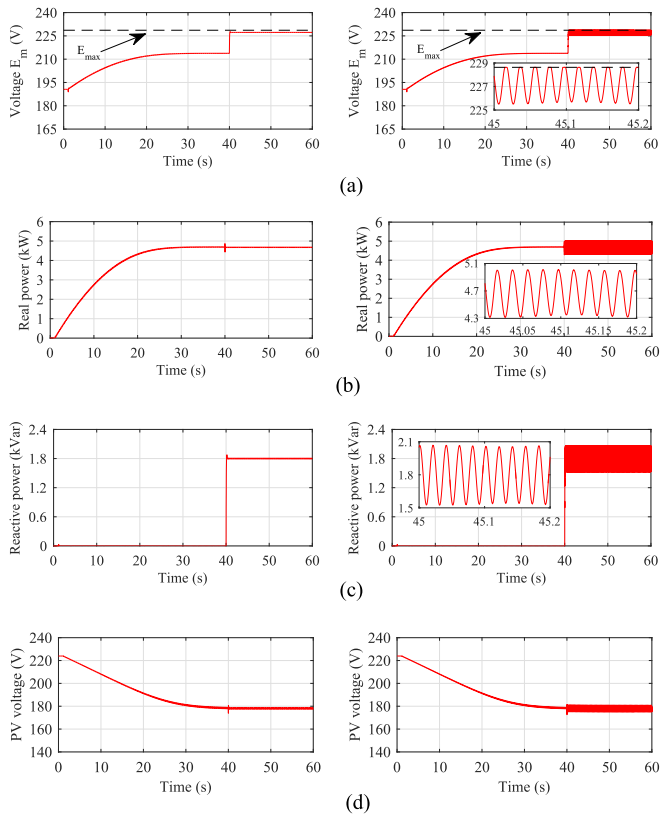


**Fig. 13.** Simulation results with bounded-voltage power flow control (left side) and with existing UDE-based power flow control [26] plus a saturation unit (right side) (Case 5). (a) Voltage  $E_m$ . (b) Real power output  $P$ . (c) Reactive power output  $Q$ . (d) PV output voltage.

The sunlight is considered as  $1000 \text{ W/m}^2$ . With the same initial settings of experimental Case 1, the MPPT is enabled after  $t = 1 \text{ s}$ . At  $t = 40 \text{ s}$ , the reactive power reference is set as  $Q^* = 1.8 \text{ kvar}$ .

The system responses are shown in Fig. 13. After enabling MPPT, the real power output in Fig. 13(b) goes up to the maximum value within 26 s in both controllers. The voltage  $E_m$  (line-line voltage) in Fig. 13(a) goes up, and PV output voltage in Fig. 13(d) goes down, accordingly. At  $t = 40 \text{ s}$ , the reactive power in Fig. 13(c) with bounded-voltage control reaches its setting 1.8 kvar quickly, and the voltage  $E_m$  is close to its maximum value  $E_{\max}$ . The real power output still keeps at the maximum value, and PV output voltage still keeps at its optimal point. There are only very small oscillations in these signals caused by perturbations from MPPT for the bounded-voltage power flow control. However, the existing UDE-based power flow control [26] with the saturation unit results in large oscillations in the voltage  $E_m$ , because the integrator windup happens when the voltage  $E_m$  is close to  $E_{\max}$ . The corresponding real power, reactive power, and PV output voltage also suffer from large oscillations. Therefore, the bounded-voltage power flow control can regulate the voltage  $E_m$  within the specific range and avoid the integrator windup caused by the saturation unit.

## VII. CONCLUSION

A new control structure was proposed in this paper for the grid-tied PV systems with the dc bus voltage regulated by the dc/dc converter controller, whereas the MPPT function, the PV voltage-regulation, and the bounded-voltage power flow control embedded into the dc/ac converter controller. This structure can guarantee voltage protection and enhance fault-ride through performance on both dc and ac sides. An UDE-based CMC was developed for the robust dc bus voltage regulation of the dc/dc converter with dc voltage protection, and the bounded-voltage power flow control provides ac voltage protection for the dc/ac converter. The effectiveness of the proposed method was experimentally validated in the lab-environment grid-tied PV system under both nominal and faulty conditions. And simulation studies have further demonstrated the advantages of the proposed method.

## ACKNOWLEDGEMENTS

The authors would like to thank Texas Instruments for the donation of inverter kits TIDM-HV-1PH-DCAC.

## REFERENCES

- [1] Q.-C. Zhong and T. Hornik, *Control of Power Inverters in Renewable Energy and Smart Grid Integration*. New York, NJ, USA: Wiley, 2013.
- [2] C. Hua, J. Lin, and C. Shen, "Implementation of a DSP-controlled photovoltaic system with peak power tracking," *IEEE Trans. Ind. Electron.*, vol. 45, no. 1, pp. 99–107, Feb. 1998.
- [3] E. Koutroulis, K. Kalaitzakis, and N. C. Voulgaris, "Development of a microcontroller-based, photovoltaic maximum power point tracking control system," *IEEE Trans. Power Electron.*, vol. 16, no. 1, pp. 46–54, Jan. 2001.
- [4] R. Leyva, C. Alonso, I. Queinnec, A. Cid-Pastor, D. Lagrange, and L. Martinez-Salamero, "MPPT of photovoltaic systems using extremum-seeking control," *IEEE Trans. Aerosp. Electron. Syst.*, vol. 42, no. 1, pp. 249–258, Jan. 2006.
- [5] N. Femia, G. Petrone, G. Spagnuolo, and M. Vitelli, "Optimization of perturb and observe maximum power point tracking method," *IEEE Trans. Power Electron.*, vol. 20, no. 4, pp. 963–973, Jul. 2005.
- [6] S. Deo, C. Jain, and B. Singh, "A PLL-less scheme for single-phase grid interfaced load compensating solar PV generation system," *IEEE Trans. Ind. Informat.*, vol. 11, no. 3, pp. 692–699, Jun. 2015.
- [7] D. G. Montoya, C. A. Ramos-Paja, and R. Giral, "Improved design of sliding-mode controllers based on the requirements of MPPT techniques," *IEEE Trans. Power Electron.*, vol. 31, no. 1, pp. 235–247, Jan. 2016.
- [8] W. Liu, K. Wang, H. Chung, and S. Chuang, "Modeling and design of series voltage compensator for reduction of DC-link capacitance in grid-tie solar inverter," *IEEE Trans. Power Electron.*, vol. 30, no. 5, pp. 2534–2548, Jul. 2015.
- [9] A. Ghaffari, M. Krstic, and S. Seshagiri, "Power optimization for photovoltaic microconverters using multivariable newton-based extremum seeking," *IEEE Trans. Control Syst. Technol.*, vol. 22, no. 6, pp. 2141–2149, Nov. 2014.
- [10] M. Killi and S. Samanta, "An adaptive voltage-sensor-based MPPT for photovoltaic systems with SEPIC converter including steady-state and drift analysis," *IEEE Trans. Ind. Electron.*, vol. 62, no. 12, pp. 7609–7619, Dec. 2015.
- [11] J. H. Teng, W. H. Huang, T. A. Hsu, and C. Y. Wang, "Novel and fast maximum power point tracking for photovoltaic generation," *IEEE Trans. Ind. Electron.*, vol. 63, no. 8, pp. 4955–4966, Aug. 2016.
- [12] N. Femia, G. Lisi, G. Petrone, G. Spagnuolo, and M. Vitelli, "Distributed maximum power point tracking of photovoltaic arrays: Novel approach and system analysis," *IEEE Trans. Ind. Electron.*, vol. 55, no. 7, pp. 2610–2621, Jul. 2008.

- [13] R. C. N. Pilawa-Podgurski and D. J. Perreault, "Submodule integrated distributed maximum power point tracking for solar photovoltaic applications," *IEEE Trans. Power Electron.*, vol. 28, no. 6, pp. 2957–2967, Jun. 2013.
- [14] E. Roman, R. Alonso, P. Ibanez, S. Elorduizapatarietxe, and D. Goitia, "Intelligent PV module for grid-connected PV systems," *IEEE Trans. Ind. Electron.*, vol. 53, no. 4, pp. 1066–1073, Jun. 2006.
- [15] C. Sreekumar and V. Agarwal, "A hybrid control algorithm for voltage regulation in DC-DC boost converter," *IEEE Trans. Ind. Electron.*, vol. 55, no. 6, pp. 2530–2538, Jun. 2008.
- [16] A. Beccuti, S. Mariethoz, S. Cliquenois, S. Wang, and M. Morari, "Explicit model predictive control of DC-DC switched-mode power supplies with extended Kalman filtering," *IEEE Trans. Ind. Electron.*, vol. 56, no. 6, pp. 1864–1874, Jun. 2009.
- [17] I. G. Zurbriggen and M. Ordonez, "Benchmarking the performance of boost-derived converters under start-up and load transients," *IEEE Trans. Ind. Electron.*, vol. 5, pp. 3125–3136, May 2016.
- [18] Q.-C. Zhong, G. C. Konstantopoulos, B. Ren, and M. Krstic, "Improved synchronverters with bounded frequency and voltage for smart grid integration," *IEEE Trans. Smart Grid*, to be published, doi: 10.1109/TSG.2016.2565663.
- [19] A. D. Paquette and D. M. Divan, "Virtual impedance current limiting for inverters in microgrids with synchronous generators," *IEEE Trans. Ind. Appl.*, vol. 51, no. 2, pp. 1630–1638, Mar. 2015.
- [20] G. C. Konstantopoulos, Q.-C. Zhong, B. Ren, and M. Krstic, "Bounded integral control of input-to-state practically stable non-linear systems to guarantee closed-loop stability," *IEEE Trans. Autom. Control*, vol. 61, no. 12, pp. 4196–4202, Dec. 2016.
- [21] Q.-C. Zhong, Z. Ma, W.-L. Ming, and G. C. Konstantopoulos, "Grid-friendly wind power systems based on the synchronverter technology," *Energy Convers. Manage.*, vol. 89, no. 1, pp. 719–726, Jan. 2015.
- [22] X. Yuan, F. Wang, D. Boroyevich, Y. Li, and R. Burgos, "DC-link voltage control of a full power converter for wind generator operating in weak-grid systems," *IEEE Trans. Power Electron.*, vol. 24, no. 9, pp. 2178–2192, Sep. 2009.
- [23] Q.-C. Zhong and D. Rees, "Control of uncertain LTI systems based on an uncertainty and disturbance estimator," *ASME Trans. J. Dyn. Sys. Meas. Control*, vol. 126, no. 4, pp. 905–910, Dec. 2004.
- [24] J. Alvarez-Ramirez, G. Espinosa-Perez, and D. Noriega-Pineda, "Current-mode control of DC-DC power converters: A backstepping approach," in *Proc. IEEE Int. Conf. Control Appl.*, Sep. 2001, pp. 190–195.
- [25] S.-K. Kim and K.-B. Lee, "Robust feedback-linearizing output voltage regulator for DC/DC boost converter," *IEEE Trans. Ind. Electron.*, vol. 62, no. 11, pp. 7127–7135, Nov. 2015.
- [26] Y. Wang, B. Ren, and Q.-C. Zhong, "Robust power flow control of grid-connected inverters," *IEEE Trans. Ind. Electron.*, vol. 63, no. 11, pp. 6887–6897, Nov. 2016.
- [27] K. B. Ariyur and M. Krstic, *Real-Time Optimization by Extremum-Seeking Control*. Hoboken, NJ, USA: Wiley-InterScience, 2003.
- [28] D. L. Evans, W. A. Facinelli, and L. P. Koehler, *Simulation and Simplified Design Studies of Photovoltaic Systems*. Springfield, VA, USA: Sandia National Laboratories, 1980.
- [29] G. Vachtsevanos and K. Kalaitzakis, "A hybrid photovoltaic simulator for utility interactive studies," *IEEE Trans. Energy Convers.*, vol. EC-2, no. 2, pp. 227–231, Jun. 1987.
- [30] 50 W polycrystalline solar panel. [Online]. Available: <https://www.renogy.com/template/files/Specifications/50-Watt-12-Volt-Polycrystalline-Solar-Panel-Specifications.pdf>
- [31] R. Naim, G. Weiss, and S. Ben-Yaakov, " $H^\infty$  control applied to boost power converters," *IEEE Trans. Power Electron.*, vol. 12, no. 4, pp. 677–683, Jul. 1997.
- [32] Q.-C. Zhong, Y. Wang, and B. Ren, "UDE-based robust droop control of inverters in parallel operation," *IEEE Trans. Ind. Electron.*, vol. 64, no. 9, pp. 7552–7562, Sep. 2017. doi: 10.1109/TIE.2017.2677309.
- [33] M. Krstić, I. Kanellakopoulos, and P. V. Kokotović, *Nonlinear and Adaptive Control Design*. New York, NJ, USA: Wiley, 1995.
- [34] Y. Qiu, H. Liu, and X. Chen, "Digital average current-mode control of PWM DC-DC converters without current sensors," *IEEE Trans. Ind. Electron.*, vol. 57, no. 5, pp. 1670–1677, May 2010.
- [35] Q. Tong, Q. Zhang, R. Min, X. Zou, Z. Liu, and Z. Chen, "Sensorless predictive peak current control for boost converter using comprehensive compensation strategy," *IEEE Trans. Ind. Electron.*, vol. 61, no. 6, pp. 2754–2766, Jun. 2014.
- [36] B. Ren, Q.-C. Zhong, and J. Dai, "Asymptotic reference tracking and disturbance rejection of UDE-based robust control," *IEEE Trans. Ind. Electron.*, vol. 64, no. 4, pp. 3166–3176, Apr. 2017.



control.

**Ye Qin Wang** (S'15) received the B.Eng. degree in automotive engineering from China Agricultural University, Beijing, China, in 2009 and the M.Eng. degree in vehicle engineering from Clean Energy Automotive Engineering Center, Tongji University, Shanghai, China, in 2012. He is currently working toward the Ph.D. degree in the National Wind Institute, Texas Tech University, Lubbock, TX, USA.

His current research interests include renewable energies, microgrids, and power electronics



**Beibei Ren** (S'05–M'10) received the B.Eng. degree in mechanical and electronic engineering and the M.Eng. degree in automation, both from Xidian University, Xi'an, China, in 2001 and in 2004, respectively, and the Ph.D. degree in electrical and computer engineering from the National University of Singapore, Singapore, in 2010.

From 2010 to 2013, she was a Postdoctoral Scholar in the Department of Mechanical and Aerospace Engineering, University of California, San Diego, CA, USA. Since 2013, she has been with the Department of Mechanical Engineering, Texas Tech University, Lubbock, TX, USA, as an Assistant Professor. Her current research interests include robust control, power electronics control, renewable energy, microgrid, and navigation and control of unmanned aerial vehicles.